NANO LETTERS

Letter

Cite This: *Nano Lett.* 2018, 18, 8016–8024

pubs.acs.org/NanoLett

Noninterleaved Metasurface for (2^6-1) Spin- and Wavelength-Encoded Holograms

Lei Jin,[†] Zhaogang Dong,[‡] Shengtao Mei,[†] Ye Feng Yu,[§] Zhun Wei,[†] Zhenying Pan,[‡,§] Soroosh Daqiqeh Rezaei,[∥,‡] Xiangping Li,[⊥] Arseniy I. Kuznetsov,[‡,§] Yuri S. Kivshar,[#] Joel K. W. Yang,[*,∇,‡] and Cheng-Wei Qiu[*,†]

[†]Department of Electrical and Computer Engineering, National University of Singapore, 4 Engineering Drive 3, Singapore 117583, Singapore

[‡]Institute of Materials Research and Engineering, A*STAR (Agency for Science, Technology and Research), 2 Fusionopolis Way, #08-03 Innovis, 138634 Singapore

[§]Data Storage Institute, A*STAR (Agency for Science, Technology and Research), 2 Fusionopolis Way, #08-01 Innovis, 138634 Singapore

[∥]Department of Mechanical Engineering, Faculty of Engineering, National University of Singapore, 9 Engineering Drive 1, 117575, Singapore

[⊥]Guangdong Provincial Key Laboratory of Optical Fiber Sensing and Communications, Institute of Photonics Technology, Jinan University, Guangzhou, 510632 China

[#]Nonlinear Physics Centre, Australian National University, Canberra ACT 2601, Australia

[∇]Singapore University of Technology and Design, 8 Somapah Road, 487372 Singapore

Supporting Information

ABSTRACT: Nanostructured metasurfaces demonstrate extraordinary capabilities to control light at the subwavelength scale, emerging as key optical components to physical realization of multitasked devices. Progress in multitasked metasurfaces has been witnessed in making a single metasurface multitasked by mainly resorting to extra spatial freedom, for example, interleaved subarrays, different angles. However, it imposes a challenge of suppressing the cross-talk among multiwavelength without the help of extra spatial freedom. Here, we introduce an entirely novel strategy of multitasked metasurfaces with noninterleaved single-size Si nanobrick arrays and minimalist spatial freedom demonstrating massive information on 6-bit encoded color holograms. The interference between electric dipole and magnetic dipole in individual Si nanobricks with in-plane orientation enables manipulating six bases of incident photons simultaneously to reconstructed 6-bit wavelength- and spin-dependent multicolor images. Those massively reconstructed images can be distinguished by pattern recognition. It opens an alternative route for integrated optics, data encoding, security encryption, and information engineering.

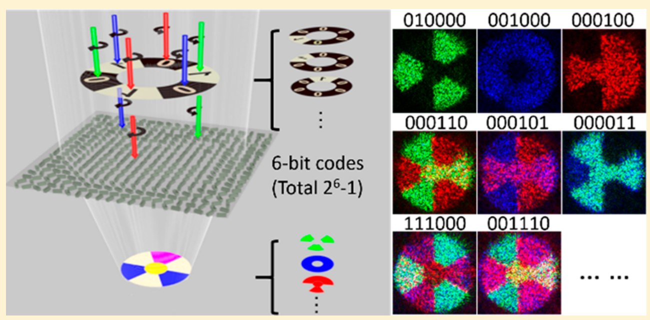

KEYWORDS: *Noninterleaved metasurface, 6-bit hologram, spin-wavelength encoding, multitasked metasurface*

Metasurfaces are engineered planar structures with subwavelength patterning to control phase, amplitude, and polarization of an optical beam.[1−6] Their operation relies on the optical response of nanostructures with position-varying parameters, allowing to shape the optical wavefront in a desirable manner.[7−22] Because of their compactness, metasurfaces are promising candidates to replace conventional optical elements such as gratings,[14,18,19] lenses,[11,20] structured beam generators,[19,21] color[6] or polarization filters,[8] and holograms[7,12,22] to miniaturize the current optical systems. Nevertheless, one physically fabricated metasurface among the literatures is normally conferred with one specific function.

The flexibility in designing metasurfaces also makes it possible to realize multitasked planar metadevices by integrating multiple functionalities into one system. The multitasked metasurfaces are mainly achieved by two approaches resorting to polarization, spatial or wavelength dimensions. The first approach is based on tailored nanostructures with polarization-selective responses. These metasurfaces with different geometries, for example, elliptical[23−26] nanostructures, cross nanostructures,[27] and nano-

Received: October 22, 2018
Revised: November 25, 2018
Published: December 6, 2018

DOI: 10.1021/acs.nanolett.8b04246
Nano Lett. 2018, 18, 8016–8024

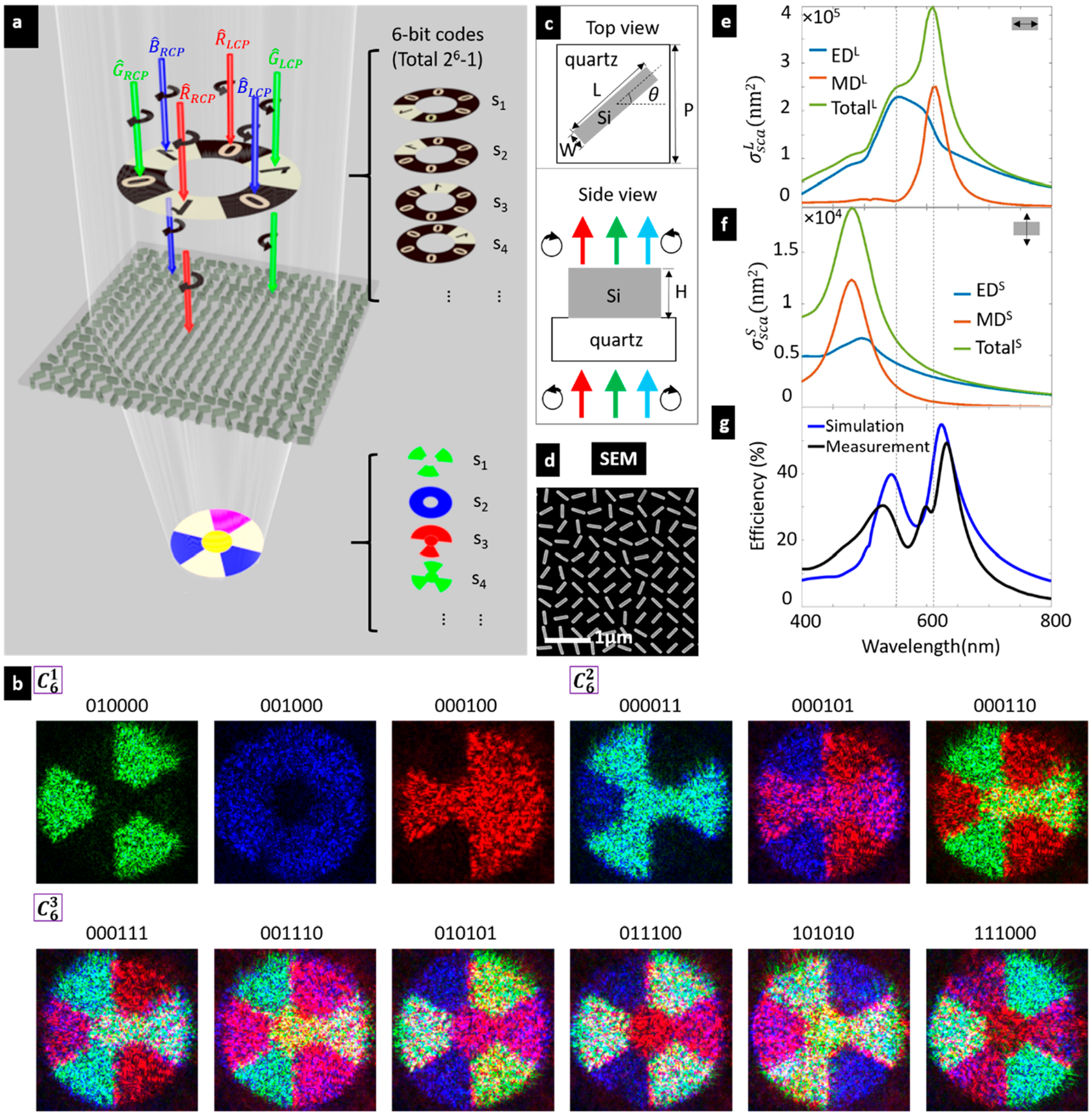

Figure 1. Schematic diagram of the mechanism and unit cell structure. (a) The transmission-type 6-bit metasurface consists of silicon nanobricks arrays with spatially varying orientations on a quartz substrate. By manipulating six fundamental bases of the input beams, the designed meta-hologram is able to reconstruct 2^6-1 different color variations of an image. The 6-bit code of the incident beam is in the transmission 1 or blocking 0 of the 3 × 2 (wavelength × spin) bases of the input light. The transmitted beams carry the embedded information on metasurface and reconstruct the corresponding images at the observation plane. The six fundamental bases ($\hat{R}_{RCP}$, $\hat{G}_{RCP}$, $\hat{B}_{RCP}$, $\hat{R}_{LCP}$, $\hat{G}_{LCP}$, and $\hat{B}_{LCP}$) of incident light are encoded by 100000, 010000, 001000, 000100, 000010, and 000001, respectively. The series s_i represent the varying states of incident beams and corresponding states of reconstructed image. (b) Part of experimental reconstructions of 6-bit metasurface by each fundamental bases (C_6^1), two out of six fundamental bases (C_6^2), and three out of six fundamental bases (C_6^3). (c) Geometry of the designed unit cell structure representing one pixel in the meta-hologram with periodicity P = 350 nm. The silicon nanobrick is 50 nm wide, 300 nm long, and 150 nm high, which rotates in plane with an orientation angle θ. The silicon nanobricks with a rotating angle will introduce the geometric phase of $\pm 2\theta$ for opposite spins. (d) Scanning electron microscopy (SEM) image of a partial region of the fabricated Si metasurface. Each Si nanobrick (300 nm × 50 nm) represents a phase pixel as defined in the metasurface (scale bar: 1 μm). The equivalent pixel size is 350 × 350 nm^2. (e,f) Multipolar decomposition calculations of the scattering cross sections, σ_{sca}^{L} (e) and σ_{sca}^{S} (f) with the superscripts denoting the polarization of the incident beam along long-axis (L) and short-axis (S) of the nanobrick, respectively. Inset: Gray rectangles are the nanobricks and double arrows are the polarizations of incident beam. (g) Simulated and measured conversion efficiency. The conversion efficiency is defined as the ratio between the optical power of the transmitted light with opposite handedness and the incident optical power. The blue and black curves represent the simulated and experimentally measured efficiency for amorphous Si nanobricks, respectively.

rods,[28−31] can achieve dual functions depending on the input polarization, such as polarization beamsplitters,[23] three-dimensional stereoscopic prints,[24] double-wavelength meta-lens,[26] and polarization-switchable holgorams.[23,27,29,31] However, capabilities of these metasurfaces are limited by polarization states. To increase the capabilities, the extra spatial freedoms were exploited. The extra spatial freedoms included multiple positions,[32−34] multiple angles,[34,35] and interleaved subarrays. For multiple positions or angles, metasurfaces controlled the incident beams to exhibits multifunctionality at different positions or angles, while interleaved was achieved either by vertical stacking[36,37] or in-plane interleaving[37−49] the subarrays specifically designed for each functionality. On the basis of the extra spatial freedoms, metasurfaces are able to generate

DOI: 10.1021/acs.nanolett.8b04246
Nano Lett. 2018, 18, 8016−8024

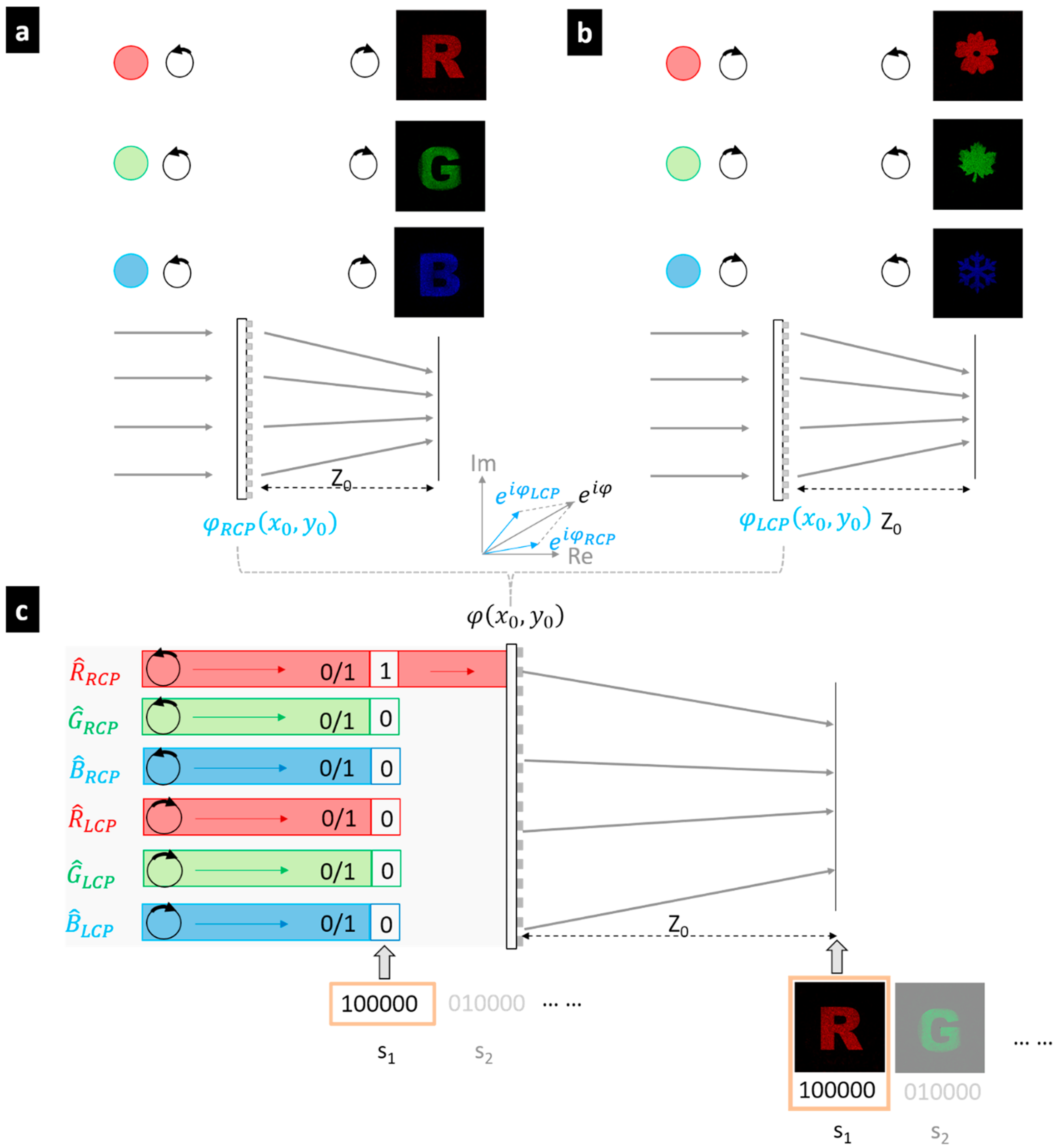

Figure 2. Creation of wavelength- and spin-dependent meta-hologram. Two sets of hologram phase profiles, $\varphi_{\rm RCP}(x_0,y_0)$ and $\varphi_{\rm LCP}(x_0,y_0)$, are designed to operate incident beams with opposite spins and merged together by the function $Ae^{i\varphi(x_0,y_0)} = e^{i\varphi_{\rm LCP}(x_0,y_0)} + e^{i\varphi_{\rm RCP}(x_0,y_0)}$. (a) Under the illumination of right-circularly polarized (RCP) light, the phase profile $\varphi_{\rm RCP}(x_0,y_0)$ reconstructs the holographic images R, G and B at the observation Z_0 plane by red, green, and blue beams, respectively. (b) Under the illumination of left-circularly polarized (LCP) light, the phase profile $\varphi_{\rm LCP}(x_0,y_0)$ reconstructs the holographic images flower, leaf, and snowflake at the observation Z_0 plane by red, green, and blue beams, respectively. (c) The designed metasurface with merged phase profile $\varphi(x_0,y_0)$ manipulates six fundamental bases to reconstruct six wavelength- and spin-dependent images at the observation Z_0 plane. The six fundamental bases are in the transmission 1 or blocking 0 state.

multimeta-hologram,[32−34,42] full-color holograms,[35,43,44,49] optical angular momentum (OAM) generators,[38,39] OAM spectropolarimeter,[40,41] optical recording,[37] and achromatic lenses.[36,46] Moreover, although wavelength dimension has been exploited for multitasked metasurfaces, the cross-talks among different wavelengths are mainly eliminated by specific tailored nanostructures,[50] multiple angles,[35] or interleaved subarrays.[43−46,49] There is a lack of a convenient way to suppress the cross-talk among multiwavelength without the help of extra spatial freedom.

In this paper, we introduce a novel type of multitasked metasurface with spin-wavelength encoding that allows 6-bit control of incident beam based on minimalist spatial freedom (noninterleaved amorphous silicon nanobricks in an on-axis system), which is capable of 6-bit encoding color holograms. Here we employ the concept of "bit" to describe the fundamental bases that reconstruct a multicolor image. Each fundamental basis represents a monochromatic beam with polarization. For a mixing beam formed by N fundamental bases, each fundamental basis can be a unit vector in N-dimensional space being expressed by an N-bit digital code. Each fundamental basis has binary states, "extinction" and "existence", corresponding to "0" and "1", respectively. To achieve the 6-bit for normal incidence, the red $\hat{R}$, green $\hat{G}$, and

DOI: 10.1021/acs.nanolett.8b04246
Nano Lett. 2018, 18, 8016−8024

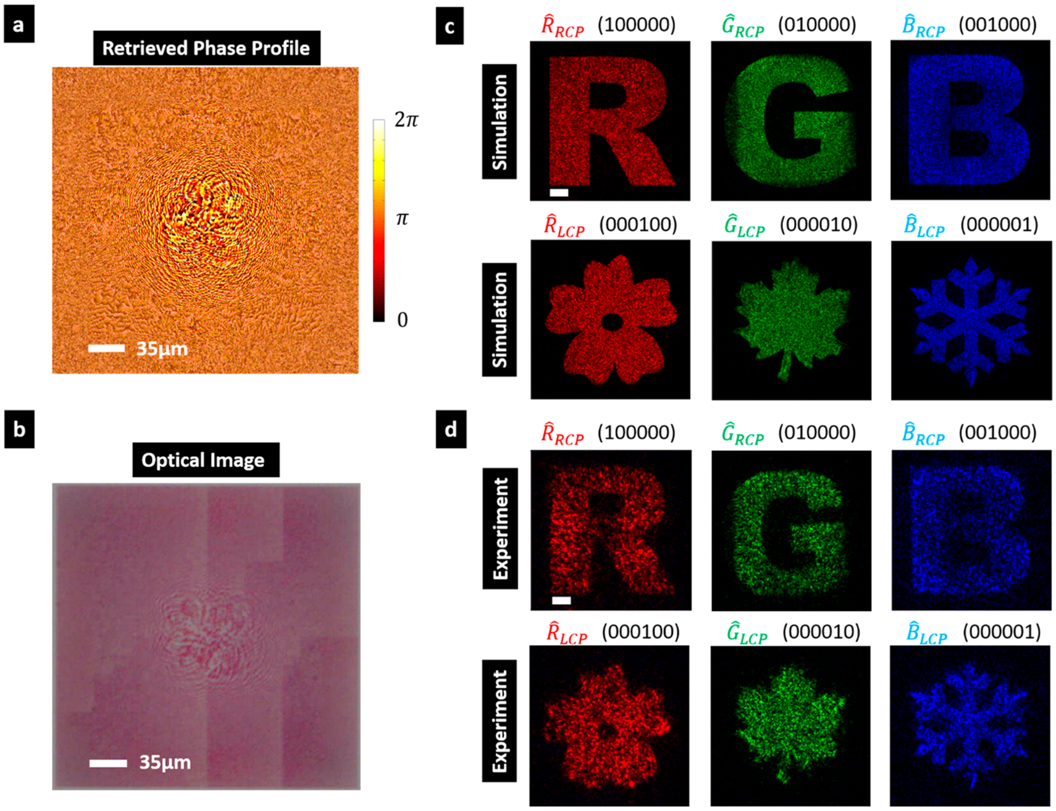

Figure 3. Demonstration of six fundamental bases for Si meta-hologram. (a) Retrieved phase profile occupying an area of 297.5 × 297.5 μm^2 consisting of an 850 × 850 pixel array. (b) Optical microscope image of the fabricated Si metasurface carrying the phase profile shown in (a). Simulated (c) and experimental (d) reconstruction of six different holograms from the designed metasurface in (b) (scale bar: 10 μm). The wavelengths of the incident light are 633, 532, and 488 nm.

blue $\hat{B}$ wavelengths with two different spins are used to represent six fundamental bases ($\hat{R}_{RCP}$, $\hat{G}_{RCP}$, $\hat{B}_{RCP}$, $\hat{R}_{LCP}$, $\hat{G}_{LCP}$, and $\hat{B}_{LCP}$). The interference between electric dipole and magnetic dipole in single-sized Si nanobricks with in-plane rotation, that is, the Pancharatnam-Berry (PB) phase, enables complete 6-bit control of incident beams, which provides the dispersionless phase profile and spin-dependent tunability. On the basis of the dispersion relationship of propagation,[46] the multiwavelength Gerchberg-Saxton (MWGS) algorithm was used to retrieve two phase profiles: one phase profile $\varphi_{RCP}(x_0,y_0)$ is designed to control $\hat{R}_{RCP}$, $\hat{G}_{RCP}$, $\hat{B}_{RCP}$ to reconstruct independent images at a given z-plane; another one $\varphi_{LCP}(x_0,y_0)$ is designed to control $\hat{R}_{LCP}$, $\hat{G}_{LCP}$, and $\hat{B}_{LCP}$ to reconstruct independent images at the same plane. These two phase profiles are then combined together by the function $Ae^{i\varphi(x_0,y_0)} = e^{i\varphi_{LCP}(x_0,y_0)} + e^{i\varphi_{RCP}(x_0,y_0)}$ and encoded into a single metasurface according to PB phase. As a result, by controlling the states of 6-bit coding incident beams, the designed 6-bit metasurface is able to reconstruct 63 spin-and wavelength-dependent holographic images (as shown in Figure 1a,b). The reconstructed images and corresponding incident beams can be distinguished by employing pattern recognition. This approach can be extended to design versatile wavelength-multiplexed planar optical devices for color display, optical imaging, optical encryption, and data encoding.

The phase-modulated 6-bit metasurface is constructed by a set of amorphous Si subwavelength elements arranged in square repeat units, that is, pixels. The local phase change of the metasurface φ is controlled by the relative orientation angle of amorphous Si nanobrick on top of the quartz substrate with the in-plane orientation θ (named PB phase), which is used to modulate the transmitted light as illustrated in Figure 1c,d. These local phase changes $\varphi(x_0,y_0) = \pm 2\theta(x_0,y_0)$ are wavelength-independent and carried by transmitted beams with opposite spins (Supporting Information Section 2). The ratio between the optical power of the transmitted light with opposite spins and the incident optical power is defined as conversion efficiency.

To achieve the total maximum conversion efficiencies at three working wavelengths (488, 532, and 633 nm), we optimize the lengths and widths of nanobricks by simulations at a fixed height of 150 nm. The width and length of silicon nanobricks are 50 and 300 nm, respectively, which are arranged on 350 nm pitch grid. Such nanobricks with high length-to-width ratio exhibit broadband localized electric dipole (ED) and magnetic dipole (MD) resonances (Figure 1e,f). The ED and MD induced by the incident beam with linear polarization along long-axis of Si nanobrick mainly contribute to the conversion efficiency (Supporting Information Section 2). As shown in Figure 1g, the measured maximum conversion efficiency is 49% at the wavelength of 633 nm. It can also be seen from Figure 1g that these nanobricks provide an acceptable conversion efficiency at the whole visible region, which broadens the working bandwidth for Si nanobricks.

The signs of these PB phase changes $\varphi(x_0,y_0) = \pm 2\theta(x_0,y_0)$ are defined by the spins of incident beams.[14] In the Fresnel region, the signs $\pm$ of the phase-only hologram $\varphi(x_0,y_0)$ lead to the real and virtual switchable holographic images with convergent and divergent wave fronts, respectively.[33] More-

DOI: 10.1021/acs.nanolett.8b04246
Nano Lett. 2018, 18, 8016−8024

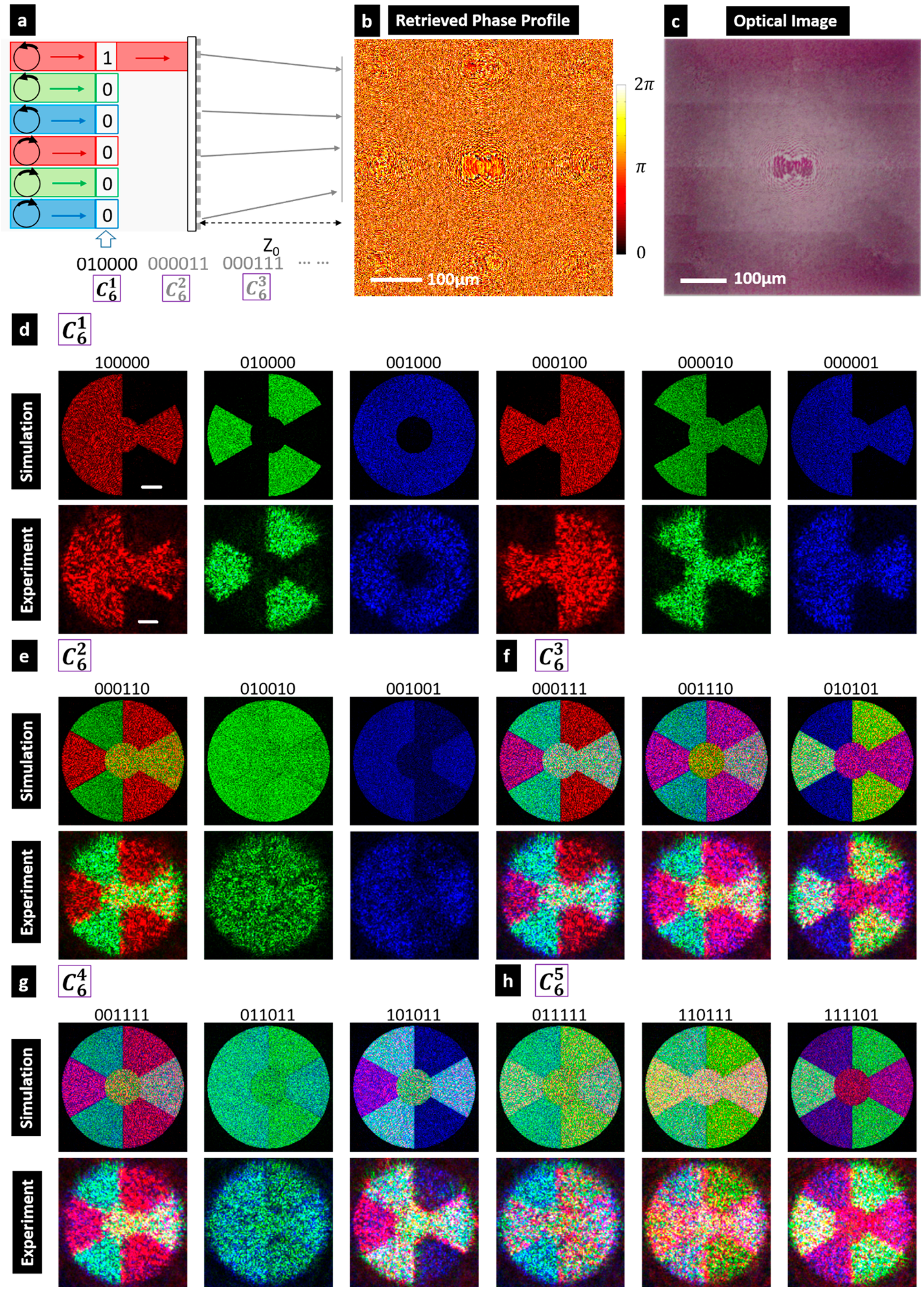

Figure 4. Reconstruction of spin- and wavelength-encoded holograms from the 6-bit metasurface with 6-bit of information. (a) Schematic illustration of the reconstructed images by each fundamental basis (fundamental states C_6^1), two out of six fundamental bases (dual states C_6^2), three out of six fundamental bases (triple states C_6^3), four out of six fundamental bases (quadruple states C_6^4), and five out of six fundamental bases (quintuple states C_6^5). (b) Designed phase profile of the 6-bit metasurface. (c) Optical microscope image of the fabricated 6-bit metasurface. Simulated (top) and measured (bottom) intensity profiles of fundamental states (d), dual states (e), triple states (f), quadruple states (g), and quintuple states (h). Scale bar, 10 μm.

over, for different working wavelengths λ these dispersionless local phase changes $\varphi(x_0,y_0)$ will reconstruct the same E-field distributions without any scaling when the product wavelength multiplying propagation distance (i.e., λz) is equal to a constant (Supporting Information Section 3). The aforementioned spin-switchable functionality and dispersion relationship

DOI: 10.1021/acs.nanolett.8b04246
Nano Lett. 2018, 18, 8016−8024

will be used to design wavelength- and spin-dependent meta-hologram.

As shown in Figure 2, to realize the wavelength- and spin-dependent meta-hologram, the key idea is to design and merge two-phase profiles, which are operating with the opposite spins of the three different monochromatic beams to reconstruct three independent images on the same plane, respectively. First, the MWGS algorithm (see detailed description in Supporting Information Section 4) is used to optimize each phase profile, which can be used to reconstruct three different independent images at the given z-plane for the three monochromatic beams (red, green, and blue). On the basis of the MWGS algorithm, we retrieve two phase profiles, $\varphi_{\mathrm{RCP}}(x_0,y_0)$ (Figure 2a) and $\varphi_{\mathrm{LCP}}(x_0,y_0)$ (Figure 2b), which respectively operates for three monochromatic beams with opposite spins to reconstruct three independent images at the same z-plane (details are shown in Supporting Information Section 5). Second, the function $Ae^{i\varphi(x_0,y_0)} = e^{i\varphi_{\mathrm{RCP}}(x_0,y_0)} + e^{i\varphi_{\mathrm{LCP}}(x_0,y_0)}$is used to merge these two phase profiles together, where the angle of this function is the merged phase profile. The final phase profile $\varphi(x_0,y_0)$ is encoded onto the metasurface, where the n^{th} phase pixel φ_n of the hologram is represented by a nanobrick with the orientation angle $\varphi_n/2$ as defined in the metasurface. As a result, (as shown in Figure, 2c) the six independent images on the same position are switchable, depending on the spins and wavelengths of the incident light. The three different monochromatic incident lights with spins can be represented as six fundamental bases ($\hat{R}_{\mathrm{RCP}}$, $\hat{G}_{\mathrm{RCP}}$, $\hat{B}_{\mathrm{RCP}}$, $\hat{R}_{\mathrm{LCP}}$, $\hat{G}_{\mathrm{LCP}}$, and $\hat{B}_{\mathrm{LCP}}$). Therefore, by arbitrarily combining the six fundamental bases of the input lights, the 6-bit metasurface with (2^6-1) spin-wavelength-encoded holograms can be realized.

Figure 3a presents the calculated phase profile for wavelength- and spin-dependent meta-hologram. In this design, a total of 722 500 nanobricks were fabricated occupying a total area of 297.5 × 297.5 μm^2. Figure 3b shows the optical microscope image of the fabricated Si metasurface. The schematic diagram of the experimental setup for the holographic reconstruction is shown in Supporting Information Section 6. The designed meta-hologram reconstructs the "R", "G", and "B" letters or the "flower", "leaf", and "snowflake" patterns at exactly the same Z position (Z_0 = 213.4 μm) for different incident wavelengths by switching the circular polarization state of the incident beam. As shown in Figure 3c, R, G, and B letters are reconstructed by red, green, and blue lasers with RCP ($\hat{R}_{\mathrm{RCP}}$,$\hat{G}_{\mathrm{RCP}}$, and $\hat{B}_{\mathrm{RCP}}$), while flower, leaf, and snowflake patterns are reconstructed by red, green, and blue lasers with LCP ($\hat{R}_{\mathrm{LCP}}$,$\hat{G}_{\mathrm{LCP}}$, and $\hat{B}_{\mathrm{LCP}}$). R, G, B, flower, leaf, and snowflake patterns correspond to the six fundamental bases, which are encoded by "100000", "010000", "001000", "000100", "000010", and "000001", respectively. Experimental results in Figure 3d restore the features of the designed images nicely with the image details. According to the image-switchable functionality, the cross-talks induced by opposite spins is switched to Z_0 = −213.4 μm. On the basis of the dispersion relationship, the similar holographic images reconstructed at different wavelengths are located in different Z planes (shown in Figures S6 and S7). Because the separation between these planes (over 14 μm) is larger than the depth of focus (DOF) of the objective used in this work (DOF is 0.91 μm), the cross-talk among different channels is eliminated at the captured plane of the charge-coupled device (CCD) camera.

The 6-bit metasurface with the massive information on (2^6-1) bits encoded in color holograms has been realized. Here, we choose a "ball" pattern as a target image, which is separated to six different images for six fundamental bases. All images are parts of the ball pattern and are reconstructed in the same plane. By arbitrarily combining the 6 fundamental bases of the input beams, the designed 6-bit metasurface can reconstruct 63 different spin- and wavelength-dependent holographic images (as shown in Figure 4a). Figure 4b,c presents the calculated phase profile and optical microscope image of the fabricated 6-bit metasurface, respectively. To characterize the 6-bit metasurface we modified the experiment setup as shown in Supporting Information Section 7. Compared to the previous setup (shown in Supporting Information Section 6), a broadband QWP is used and the circular polarization analyzer before the CCD camera is removed, which introduces additional noise to the holographic projections.

Figure 4d demonstrates the simulated and measured results of the reconstructed images of the fundamental states. As expected, the holograms generate images with the identical size and position for the given wavelength. By selecting the fundamental bases, the fundamental states of the reconstructed images can be switched. Thanks to the identical position of the reconstructed images, the designed 6-bit metasurface can provide the compound states of the reconstructed images by controlling the combination of the six fundamental bases of the input light. By choosing two out of three monochromatic incident beams with circular polarizations, the dual states enable not only the primary colors (RGB) but also their secondary colors (cyan, magenta and yellow), as shown in Figure, 4e. When one monochromatic beam with a linear polarization (i.e., RCP + LCP) illuminates the designed 6-bit metasurface, the reconstructed image ball with primary colors (i.e., RGB) can be achieved at the observation plane. In addition, Figure 4f presents a part of the intensity profiles of the triple states. When the metasurface is illuminated by three beams with different wavelengths and spins simultaneously, the corresponding triple state shows a full-color (including white) reconstructed image at the observation plane.

The designed metasurface also could support quadruple states and quintuple states, which are shown in Figure 4g,h, respectively. By arbitrarily combining the 6 fundamental bases of the input light, massive information on 63 spin- and wavelength-dependent holographic images can be achieved as shown in Supporting Information Section 8. The measured intensity profiles of each state show great fidelity with the colors, shapes, and sizes of the simulated intensity profiles. The 6-bit digital code of each intensity profile can be distinguished by employing correlation functions (Supporting Information Section 9), and the information on incident beam can consequently be uniquely determined from the code.

The diffraction efficiency is a critical issue related to the multitasked meta-holograms with massive information. We provide a comparison between our noninterleaved method and spatial multiplexed method (Supporting Information Section 10) concerning the diffraction efficiency. The diffraction efficiency is defined as the ratio between the power of the reconstructed monochromatic image and the power of the converted transmitted light.[51] Here, the reconstructed images of different bits are located at the different areas in the same plane. Figure S12 shows the average diffraction efficiency of

DOI: 10.1021/acs.nanolett.8b04246
Nano Lett. 2018, 18, 8016−8024

spatial multiplexed method decreases according to $1/N^2$,[41] where N is the number of bit. Compared with spatial multiplexed method, the higher average diffraction efficiencies of noninterleaved method are achieved, because noninterleaved method is based on harmonic response.[41] Moreover, if the reconstructed images move to the same area, noninterleaved metasurface will control the composite wavefront near the optical axis without separation, which is able to further improve the energy utilization.

In this work, the designed multitasked metasurface is used to control six fundamental bases of incidences. To estimate the capacity of a multitasked noninterleaved metasurface, additional fundamental bases of beams at different wavelengths are involved in the metasuraface design and the signal-to-noise ratio (SNR) is used to evaluate the quality of reconstructed images (Supporting Information Section 10). The SNR is defined by the ratio the between the peak intensity in the reconstructed image and the standard deviation of the background noise.[51] Figure S13 shows that as the number of bit increases to 14, even though the average SNR reduces to about 40, the reconstructions by each fundamental bases are still recognizable. This introduction of additional fundamental bases will remarkably increase the information states carried by a single metasurface.

In summary, we present a unique approach for achieving the 6-bit metasurface capable of encoding (2^6-1) color holograms based on an array of noninterleaved amorphous Si nanobricks. These massive reconstructed holograms are arisen from superposition and permutation of six fundamental independent images. This approach not only overcome the cross-talk limitation by single size elements for on-axis illumination but also realizes a high-capability metasurface with great image quality. It provides a way for future practical devices with multiwavelength functionalities that may lead to advances in a wide range of fields such as color display, information encryption, and beam characterization.

Sample Fabrication. The sample was fabricated by a conventional electron beam lithography (EBL). Amorphous silicon thin films were deposited on fused silica substrates by using chemical vapor deposition (Oxford PECVD). The samples were then spin coated a layer of hydrogen silsesquioxane (HSQ, Dow Corning(R) XR-1541-006) and a charge-dissipation layer (Espacer 300Z) for EBL(Elionix ELS-7000) patterning (acceleration voltage of 100 keV, e-beam current of 200 pA, and exposure dose of 12 mC cm^{-2}[52]). After the exposure, the samples were first rinsed in DI water to remove the Espacer and then developed in the salty developer solution[52] for 1 min, followed by DI water, acetone/IPA rinsing, and blow dry. The samples were finally etched by reactive-ion-etching in inductively coupled plasma system (Oxford Plasmalab 100) with the following recipe: Cl_2 with a flow rate of 22 sccm, ICP power of 400 W, RIE power of 100 W, and temperature of 6 °C.

Numerical Simulations. Lumerical FDTD Solution (a commercial software) was used to simulate and optimize the elements of the metasurface. In this simulation, periodic boundary conditions were employed along x- and y-directions, while perfect matched layer was used along z-direction. The circular polarized light is formed by two sources polarized along x-and y-axes with a phase shift of ±90°, and the circularly polarized beam is normally incident onto the nanobricks from the substrate side. Experimentally measured refraction index of amorphous Si is used in the simulations (Supporting Information Section 1). The multipole decomposition is calculated by the Cartesian multipole analysis based on the electric field within the Si nanobricks.[17,53,54]

■ ASSOCIATED CONTENT

Supporting Information

The Supporting Information is available free of charge on the ACS Publications website at DOI: 10.1021/acs.nanolett.8b04246.

> Material properties used for the simulation, PB phase introduced by nanobrick, dispersion relationship, multi-wavelength Gerchberg-Saxton algorithm, detailed illustration of phase profiles, experimental setup for characterization of the spin and wavelength multiplexed Si hologram, experimental setup for characterization of the 6-bit metasurface, reconstruction of 63 spin- and wavelength-dependent holographic images from the 6-bit metasurface, pattern recognition, diffraction efficiency and signal-to-noise ratio (PDF)

■ AUTHOR INFORMATION

Corresponding Authors

*(C.-W.Q.) E-mail: chengwei.qiu@nus.edu.sg. Telephone: +65 65162559.

*(J.K.W.Y.) E-mail: joel_yang@sutd.edu.sg. Telephone: +65 64994767.

ORCID

Zhaogang Dong: 0000-0002-0929-7723
Xiangping Li: 0000-0003-0955-2613
Arseniy I. Kuznetsov: 0000-0002-7622-8939
Yuri S. Kivshar: 0000-0002-3410-812X
Joel K. W. Yang: 0000-0003-3301-1040
Cheng-Wei Qiu: 0000-0002-6605-500X

Author Contributions

L.J. and Z.D. contributed equally to this work. L.J., Z.D., S.M., J.K.W.Y. and C.W.Q. conceived the idea. L.J. and C.W.Q. designed the hologram nanostructures and did the optical characterization of the hologram. Z.D. and J.K.W.Y did the nanofabrication of the silicon nanostructures. Y.F.Y. did the growth of amorphous silicon by using PECVD method. Z.W. provides the expertise knowledge on the Gerchberg-Saxton algorithm and pattern recognition. Z.D. and Z.P. did the dry etching of silicon by using the inductively coupled plasma. S.D.R. did the multipole decomposition. X.L., A.I.K. and Y.K. participated in the discussions and contributed with valuable suggestions for silicon metasurface holograms. The paper was drafted by L.J. with inputs from Z.D., J.K.W.Y. and C.W.Q. All authors analyzed the data, read and corrected the manuscript before the manuscript submission. C.W.Q. and J.K.W.Y. supervised the project.

Notes

The authors declare no competing financial interest.

■ ACKNOWLEDGMENTS

C.-W.Q. acknowledges the financial support from the National Research Foundation, Prime Minister's Office, Singapore under its Competitive Research Program (CRP award NRF-CRP15-2015-03). Z.D., Y.F.Y., Z.P., A.I.K., and J.K.W.Y. would like to acknowledge the funding support from Agency for Science, Technology and Research (A*STAR) SERC Pharos project (Grant 1527300025). In addition, Z.D. and J.K.W.Y.

DOI: 10.1021/acs.nanolett.8b04246
Nano Lett. 2018, 18, 8016−8024

also acknowledge the funding support from A*STAR Young Investigatorship (Grant 0926030138), SERC (Grant 092154099), National Research Foundation Grant Award No. NRF-CRP001-021, NRF-CRP 8-2011-07, and A*STAR-JCO under project number 1437C00135. X.L. acknowledges National Natural Science Foundation of China (NSFC) (Grant 61522504) and Guangdong Provincial Innovation and Entrepreneurship Project (Grant 2016ZT06D081).

■ ABBREVIATIONS

PB phase, Pancharatnam-Berry phase; MWGS, algorith mmulti-wavelength Gerchberg-Saxton algorithm; ED, electric dipole; MD, magnetic dipole; RCP, right-circularly polarized; LCP, left-circularly polarized SNR signal-to-noise ratio.

■ REFERENCES

(1) Yu, N.; Genevet, P.; Kats, M. A.; Aieta, F.; Tetienne, J. P.; Capasso, F.; Gaburro, Z. *Science* **2011**, *334*, 333−337.
(2) Yu, N.; Capasso, F. *Nat. Mater.* **2014**, *13*, 139−150.
(3) Kildishev, A. V.; Boltasseva, A.; Shalaev, V. M. *Science* **2013**, *339*, 1232009.
(4) Levy, U.; Abashin, M.; Ikeda, K.; Krishnamoorthy, A.; Cunningham, J.; Fainman, Y. *Phys. Rev. Lett.* **2007**, *98*, 243901.
(5) Zhu, A. Y.; Kuznetsov, A. I.; Luk'yanchuk, B.; Engheta, N.; Genevet, P. *Nanophotonics* **2017**, *6*, 452.
(6) Kristensen, A.; Yang, J. K.; Bozhevolnyi, S. I.; Link, S.; Nordlander, P.; Halas, N. J.; Mortensen, N. A. *Nat. Rev. Mater.* **2017**, *2*, 16088.
(7) Zheng, G.; Mühlenbernd, H.; Kenney, M.; Li, G.; Zentgraf, T.; Zhang, S. *Nat. Nanotechnol.* **2015**, *10*, 308−312.
(8) Wu, P. C.; Tsai, W. Y.; Chen, W. T.; Huang, Y. W.; Chen, T. Y.; Chen, J. W.; Liao, C. Y.; Chu, C. H.; Sun, G.; Tsai, D. P. *Nano Lett.* **2017**, *17*, 445−452.
(9) Gu, Y.; Zhang, L.; Yang, J. K.; Yeo, S. P.; Qiu, C. W. *Nanoscale* **2015**, *7*, 6409−6419.
(10) Zhou, Z.; Li, J.; Su, R.; Yao, B.; Fang, H.; Li, K.; Zhou, L.; Liu, J.; Stellinga, D.; Reardon, C. P.; Krauss, T. F.; Wang, X. *ACS Photonics* **2017**, *4*, 544−551.
(11) Paniagua-Dominguez, R.; Yu, Y. F.; Khaidarov, E.; Choi, S.; Leong, V.; Bakker, R. M.; Liang, X.; Fu, Y. H.; Valuckas, V.; Krivitsky, L. A.; Kuznetsov, A. I. *Nano Lett.* **2018**, *18*, 2124−2132.
(12) Huang, K.; Liu, H.; Garcia-Vidal, F. J.; Hong, M.; Luk'yanchuk, B.; Teng, J.; Qiu, C. W. *Nat. Commun.* **2015**, *6*, 7059.
(13) Zhang, X.; Tian, Z.; Yue, W.; Gu, J.; Zhang, S.; Han, J.; Zhang, W. *Adv. Mater.* **2013**, *25*, 4567−4572.
(14) Huang, L.; Chen, X.; Mühlenbernd, H.; Li, G.; Bai, B.; Tan, Q.; Jin, G.; Zentgraf, T.; Zhang, S. *Nano Lett.* **2012**, *12*, 5750−5755.
(15) Paniagua-Domínguez, R.; Yu, Y. F.; Miroshnichenko, A. E.; Krivitsky, L. A.; Fu, Y. H.; Valuckas, V.; Gonzaga, L.; Toh, Y. T.; Kay, A. Y. S.; Luk'yanchuk, B.; Kuznetsov, A. I. *Nat. Commun.* **2016**, *7*, 10362.
(16) Ye, W.; Zeuner, F.; Li, X.; Reineke, B.; He, S.; Qiu, C. W.; Liu, J.; Wang, Y.; Zhang, S.; Zentgraf, T. *Nat. Commun.* **2016**, *7*, 11930.
(17) Dong, Z.; Ho, J.; Yu, Y. F.; Fu, Y. H.; Paniagua-Dominguez, R.; Wang, S.; Kuznetsov, A. I.; Yang, J. K. *Nano Lett.* **2017**, *17* (12), 7620−7628.
(18) Karagodsky, V.; Chang-Hasnain, C. *Opt. Express* **2012**, *20* (10), 10888−10895.
(19) Li, K.; Ran, Y.; Chase, C.; Yang, W.; Chang-Hasnain, C. J. *Optica* **2018**, *5*, 10−13.
(20) Lalanne, P.; Chavel, P. *Laser Photon. Rev.* **2017**, *11*, 1600295.
(21) Devlin, R. C.; Ambrosio, A.; Wintz, D.; Oscurato, S. L.; Zhu, A. Y.; Khorasaninejad, M.; Oh, J.; Maddalena, P.; Capasso, F. *Opt. Express* **2017**, *25*, 377−393.
(22) Wang, L.; Kruk, S.; Tang, H.; Li, T.; Kravchenko, I.; Neshev, D. N.; Kivshar, Y. S. *Optica* **2016**, *3*, 1504.
(23) Arbabi, A.; Horie, Y.; Bagheri, M.; Faraon, A. *Nat. Nanotechnol.* **2015**, *10*, 937−943.
(24) Goh, X. M.; Zheng, Y.; Tan, S. J.; Zhang, L.; Kumar, K.; Qiu, C. W.; Yang, J. K. *Nat. Commun.* **2014**, *5*, 5361.
(25) Kruk, S.; Hopkins, B.; Kravchenko, I. I.; Miroshnichenko, A.; Neshev, D. N.; Kivshar, Y. S. *APL Photonics* **2016**, *1*, 030801.
(26) Arbabi, E.; Arbabi, A.; Kamali, S. M.; Horie, Y.; Faraon, A. *Opt. Express* **2016**, *24*, 18468−18477.
(27) Chen, W. T.; Yang, K. Y.; Wang, C. M.; Huang, Y. W.; Sun, G.; Chiang, I. D.; Liao, C. Y.; Hsu, W. L.; Lin, H. T.; Sun, S.; Zhou, L.; Liu, A. Q.; Tsai, D. P. *Nano Lett.* **2014**, *14*, 225−230.
(28) Khorasaninejad, M.; Chen, W. T.; Zhu, A. Y.; Oh, J.; Devlin, R. C.; Rousso, D.; Capasso, F. *Nano Lett.* **2016**, *16*, 4595−4600.
(29) Montelongo, Y.; Tenorio-Pearl, J. O.; Milne, W. I.; Wilkinson, T. D. *Nano Lett.* **2014**, *14*, 294−298.
(30) Zhou, J.; Qian, H.; Hu, G.; Luo, H.; Wen, S.; Liu, Z. *ACS Nano* **2018**, *12*, 82−88.
(31) Balthasar Mueller, J. B.; Rubin, N. A.; Devlin, R. C.; Groever, B.; Capasso, F. *Phys. Rev. Lett.* **2017**, *118*, 113901.
(32) Levy, U.; Marom, E.; Mendlovic, D. *Opt. Lett.* **2001**, *26* (15), 1149−1151.
(33) Huang, K.; Dong, Z.; Mei, S.; Zhang, L.; Liu, Y.; Liu, H.; Zhu, H.; Teng, J.; Luk'yanchuk, B.; Yang, J. K.; Qiu, C. W. *Laser Photonics Rev.* **2016**, *10*, 500−509.
(34) Huang, L.; Mühlenbernd, H.; Li, X.; Song, X.; Bai, B.; Wang, Y.; Zentgraf, T. *Adv. Mater.* **2015**, *27*, 6444−6449.
(35) Li, X.; Chen, L.; Li, Y.; Zhang, X.; Pu, M.; Zhao, Z.; Ma, X.; Wang, Y.; Hong, M.; Luo, X. *Sci. Adv.* **2016**, *2*, No. e1601102.
(36) Avayu, O.; Almeida, E.; Prior, Y.; Ellenbogen, T. *Nat. Commun.* **2017**, *8*, 14992.
(37) Zijlstra, P.; Chon, J. W. M.; Gu, M. *Nature* **2009**, *459*, 410−413.
(38) Mei, S.; Mehmood, M. Q.; Hussain, S.; Huang, K.; Ling, X.; Siew, S. Y.; Liu, H.; Teng, J.; Danner, A.; Qiu, C. W. *Adv. Funct. Mater.* **2016**, *26*, 5255.
(39) Mehmood, M. Q.; Mei, S.; Hussain, S.; Huang, K.; Siew, S. Y.; Zhang, L.; Zhang, T.; Ling, X.; Liu, H.; Teng, J.; Danner, A.; Zhang, S.; Qiu, C.-W. *Adv. Mater.* **2016**, *28*, 2533.
(40) Maguid, E.; Yulevich, I.; Yannai, M.; Kleiner, V.; Brongersma, M. L.; Hasman, E. *Light: Sci. Appl.* **2017**, *6*, No. e17027.
(41) Maguid, E.; Yulevich, I.; Veksler, D.; Kleiner, V.; Brongersma, M. L.; Hasman, E. *Science* **2016**, *352*, 1202.
(42) Zhang, C.; Yue, F.; Wen, D.; Chen, M.; Zhang, Z.; Wang, W.; Chen, X. *ACS Photonics* **2017**, *4*, 1906−1912.
(43) Huang, Y. W.; Chen, W. T.; Tsai, W. Y.; Wu, P. C.; Wang, C. M.; Sun, G.; Tsai, D. P. *Nano Lett.* **2015**, *15*, 3122−3127.
(44) Wang, B.; Dong, F.; Li, Q. T.; Yang, D.; Sun, C.; Chen, J.; Song, Z.; Xu, L.; Chu, W.; Xiao, Y. F.; Gong, Q.; Li, Y. *Nano Lett.* **2016**, *16*, 5235−5240.
(45) Zhao, W.; Liu, B.; Jiang, H.; Song, J.; Pei, Y.; Jiang, Y. *Opt. Lett.* **2016**, *41*, 147−150.
(46) Li, K.; Guo, Y.; Pu, M.; Li, X.; Ma, X.; Zhao, Z.; Luo, X. *Opt. Express* **2017**, *25*, 21419.
(47) Deng, Z. L.; Deng, J.; Zhuang, X.; Wang, S.; Li, K.; Wang, Y.; Chi, Y.; Ye, X.; Xu, J.; Wang, G. P.; Zhao, R.; Wang, X.; Cao, Y.; Cheng, X.; Li, G.; Li, X. *Nano Lett.* **2018**, *18*, 2885−2892.
(48) Wang, K.; Titchener, J. G.; Kruk, S. S.; Xu, L.; Chung, H. P.; Parry, M.; Kravchenko, I. I.; Chen, Y. H.; Solntsev, A. S.; Kivshar, Y. S.; Neshev, D. N.; Sukhorukov, A. A. *Science* **2018**, *361*, 1104−1108.
(49) Dong, F.; Feng, H.; Xu, L.; Wang, B.; Song, Z.; Zhang, X.; Li, L. Y. X.; Sun, L. F.; Li, Y.; Chu, W. *arXiv* **2018**, 1805.11246.
(50) Shi, Z.; Khorasaninejad, M.; Huang, Y. W.; Roques-Carmes, C.; Zhu, A. Y.; Chen, W. T.; Sanjeev, V.; Ding, Z. W.; Tamagnone, M.; Chaudhary, K.; Devlin, R. C.; Qiu, C. W.; Capasso, F. *Nano Lett.* **2018**, *18* (4), 2420−2427.
(51) Ni, X.; Kildishev, A. V.; Shalaev, V. M. *Nat. Commun.* **2013**, *4*, 2807.

DOI: 10.1021/acs.nanolett.8b04246
Nano Lett. 2018, 18, 8016−8024

(52) Dong, Z.; Asbahi, M.; Lin, J.; Zhu, D.; Wang, Y. M.; Hippalgaonkar, K.; Chu, H. S.; Goh, W. P.; Wang, F.; Huang, Z.; Yang, J. K. *Nano Lett.* **2015**, *15*, 5976−5981.

(53) Evlyukhin, A. B.; Reinhardt, C.; Evlyukhin, E.; Chichkov, B. N. *J. Opt. Soc. Am. B* **2013**, *30*, 2589−2598.

(54) Yang, Y.; Miroshnichenko, A. E.; Kostinski, S. V.; Odit, M.; Kapitanova, P.; Qiu, M.; Kivshar, Y. S. *Phys. Rev. B: Condens. Matter Mater. Phys.* **2017**, *95*, 165426.

DOI: 10.1021/acs.nanolett.8b04246
Nano Lett. 2018, 18, 8016−8024